

IPA. Accretion rate of a low-mass Class 0 protostar, measured via mid-infrared fluorescent OH emission

DAN M. WATSON ¹, MAYANK NARANG ^{2,3}, CAELEY V. PITTMAN ^{4,5}, HIMANSHU TYAGI ⁶, ROBERT GUTERMUTH ⁷,
 ADAM E. RUBINSTEIN ¹, NEAL J. EVANS II ⁸, LEE W. HARTMANN ⁹, S. THOMAS MEGEATH ¹⁰, P. MANOJ ⁶,
 CATHERINE C. ESPAILLAT ^{4,5}, NURIA CALVET ⁹, ALESSIO CARATTI O GARATTI ¹¹, EWINE F. VAN DISHOECK ¹²,
 TYLER L. BOURKE ¹³, JOEL D. GREEN ¹⁴, CAREY M. LISSE ¹⁵, PAMELA KLAASSEN ¹⁶, LESLIE W. LOONEY ¹⁷,
 POONEH NAZARI ^{12,18}, DAVID A. NEUFELD ¹⁹, JOHN J. TOBIN ²⁰, SCOTT J. WOLK ²¹, GUILLEM ANGLADA ²²,
 PRABHANI ATNAGULOV ²³, HENRIK BEUTHER ²⁴, NASHANTY G. C. BRUNKEN ¹², SAMUEL FEDERMAN ^{10,25},
 ELISE FURLAN ²⁶, NOLAN HABEL ², NICOLE KARNATH ²⁷, HENDRIK LINZ ²⁴, JAMES MUZEROLLE PAGE ¹⁴,
 MAYRA OSORIO ²², RIWAJ POKHREL ²⁸, ROHAN RAHATGAONKAR ²⁹, WILL R. M. ROCHA ¹²,
 PATRICK D. SHEEHAN ³⁰, KATERINA SLAVICINSKA ¹², THOMAS STANKE ³¹, AMELIA M. STUTZ ³²,
 LUKASZ TYCHONIEC ³³, YAO-LUN YANG ³⁴ AND WILLIAM J. FISCHER ¹⁴

¹Department of Physics and Astronomy, University of Rochester, Rochester, NY 14627, USA

²Jet Propulsion Laboratory, California Institute of Technology, 4800 Oak Grove Drive, Pasadena, CA 91109, USA

³Academia Sinica Institute of Astronomy & Astrophysics, Taipei 10617, TW, R.O.C.

⁴Department of Astronomy, Boston University, 725 Commonwealth Avenue, Boston, MA 02215, USA

⁵Institute for Astrophysical Research, Boston University, 725 Commonwealth Avenue, Boston, MA 02215, USA

⁶Department of Astronomy & Astrophysics Tata Institute of Fundamental Research, Colaba, Mumbai, Maharashtra, IN

⁷Department of Astronomy, University of Massachusetts Amherst, Amherst, MA 01003, USA

⁸Department of Astronomy, University of Texas at Austin, Austin, TX 78712, USA

⁹Department of Astronomy, University of Michigan – Ann Arbor, Ann Arbor, MI 48109, USA

¹⁰Ritter Astrophysical Research Center, Department of Physics and Astronomy, University of Toledo, Toledo, OH 43606, USA

¹¹INAF - Osservatorio Astronomico di Capodimonte, via Moiariello 16, 80131 Napoli, Italy

¹²Leiden Observatory, Leiden University, 2300 RA Leiden, South Holland, NL

¹³SKA Observatory, Jodrell Bank, Lower Withington, Macclesfield SK11 9FT, UK

¹⁴Space Telescope Science Institute, Baltimore, MD 21218, USA

¹⁵Planetary Exploration Group, Space Department, Johns Hopkins University Applied Physics Laboratory, Laurel, MD 2072

¹⁶United Kingdom Astronomy Technology Centre, Royal Observatory Edinburgh, Blackford Hill, Edinburgh EH9 3HJ, UK

¹⁷Department of Astronomy, University of Illinois, Urbana, IL 61801, USA

¹⁸European Southern Observatory, 85748 Garching, DE

¹⁹William H. Miller III Department of Physics and Astronomy, The Johns Hopkins University, Baltimore, MD, USA

²⁰National Radio Astronomy Observatory, Charlottesville, VA 22903, USA

²¹Harvard-Smithsonian Center for Astrophysics, Cambridge, MA 02138, USA

²²Instituto de Astrofísica de Andalucía, CSIC, Glorieta de la Astronomía s/n, E-18008 Granada, ES

²³Ritter Astrophysical Research Center, Dept. of Physics and Astronomy, University of Toledo, Toledo, OH, USA

²⁴Max Planck Institute for Astronomy, Heidelberg, Baden-Württemberg, DE

²⁵INAF-Osservatorio Astronomico di Capodimonte, IT

²⁶Caltech/IPAC-NASA Exoplanet Science Institute, Pasadena, CA 91106, USA

²⁷Space Science Institute, Boulder, CO 80301, USA

²⁸Ritter Astrophysical Research Center, Dept. of Physics and Astronomy, University of Toledo, Toledo, OH 43606, USA

²⁹Gemini South Observatory, La Serena, CL

³⁰National Radio Astronomy Observatory, Charlottesville, VA 22903 USA

³¹Max Planck Institute for Extraterrestrial Physics, Gießenbachstraße 185748 Garching, DE

³²Departamento de Astronomía, Universidad de Concepción, Concepción, CL

³³European Southern Observatory, Garching bei München, DE

³⁴RIKEN Cluster for Pioneering Research, Wako-shi, Saitama, 351-0106, JP

ABSTRACT

The earliest stages of star formation are highlighted by complex interactions between accretion, outflow, and radiative processes, which shape the chemical and physical environment of the emerging protostar. James Webb Space Telescope observations of the low-mass, low-luminosity Class 0 protostar

IRAS 16253-2429 reveal a central compact source. This object exhibits a rich mid-infrared emission spectrum of OH pure rotational lines and CO₂ ro-vibrational lines. Unusually for a young stellar object, it has no mid-infrared line emission from H₂O to match the other molecules. We demonstrate that the emitting OH molecules arise from UV photodissociation of H₂O in its second absorption band at $\lambda = 114 - 145$ nm, and that the OH emission is a fluorescent cascade starting with highest-excitation rotational states. This situation offers the opportunity of using the infrared OH spectrum to measure the UV flux from the central protostar. Thereby we determine the disk-star accretion rate to be $3 \times 10^{-10} M_{\odot}$ year⁻¹, and demonstrate that the system luminosity arises mostly from the protostar's photosphere rather than from accretion luminosity. The result is in accord with the measured outflow rate of IRAS 16253-2429 and lies within the outflow/accretion-flow rate trend often inferred for protostars; and with episodic accretion as the dominant mechanism by which this protostar has grown.

Keywords: Protostars (1302), Protoplanetary disks (1300), Star formation (1569)

1. DEDICATION

We dedicate this article to the memory of our colleague William J. Fischer, who passed away tragically on 16 April 2024, in the prime of his life and career. Will was well known for his work on star formation, the evolution of young stars, and especially for infrared and UV studies of accretion processes. Most of us have worked closely with Will for more than a decade; he was a great teammate and a great friend, and his death is a profound loss.

2. INTRODUCTION

Mass assembly in low-mass protostars is thought to occur via the infall of gas onto a disk and the subsequent accretion of that gas from the disk to star (e.g. Hartmann et al. 2016). Measurements of the disk to star accretion rate, \dot{M}_a , are therefore fundamental to studies of protostellar evolution. Among several ways to measure \dot{M}_a , the best is *via* ultraviolet excess: namely, continuum and line emission in excess of the protostar's photosphere (e.g., Hartmann 2009). The excess arises mostly in shocked gas, energized by impact of disk material as it falls from several stellar radii away (Calvet & Gullbring 1998, Pittman et al. 2025). The main difficulty in direct measurement of UV excess is extinction in the foreground of the star. This hindrance is merely significant for Class II young stellar objects (YSOs), but becomes insuperable for the spectral-energy-distribution classes (0, I, flat-spectrum) characteristic of early evolutionary stages. Supplementary methods, based on empirical relationships between near-infrared H I recombination line fluxes and accretion luminosity (e.g. Muzerolle et al. 1998, Alcalá et al. 2014, Alcalá et al. 2017, Komarova & Fischer 2020, Fiorellino et al. 2023, Tofflemire et al. 2025, Testi et al. 2025), extend our grasp into this envelope-dominated range, though they are difficult to

use if envelope extinction is very large (Le Gouellec et al. 2024), if accretion occurs through a disk boundary layer (Hartmann et al. 2016, Fischer et al. 2012), or if substantial H I emission arises from processes related to outflows (e.g. Narang et al. 2024, Federman et al. 2024).

Here we present a different method, of promise for low-mass YSOs in these early stages: photodissociation of water in the inner regions of protostars, within range of the star's accretion-generated ultraviolet. Hydroxyl (OH) radicals produced thereby emit a fluorescent cascade in the mid infrared ($\lambda > 5 \mu\text{m}$). The OH emission is directly dependent upon the UV luminosity and the rate of mass accretion that produced it.

We apply this novel method to IRAS 16253-2429 (henceforth I16253), a Class 0 protostar in the main Ophiuchus/L1688 molecular cloud. I16253's bolometric luminosity is $L_{bol} = 0.16 L_{\odot}$ at distance $d_0 = 140$ pc (Aso et al. 2023, Pokhrel et al. 2023). The central star's mass is determined kinematically to be $M = 0.15 \pm 0.03 M_{\odot}$ (Aso et al. 2023, Hsieh et al. 2019). Its protostellar envelope is large by comparison, at $M_{env} = 1.0 \pm 0.5 M_{\odot}$ (Young et al. 2006, Tobin et al. 2011), and infall motions are detected in the envelope's inner parts (Aso et al. 2023). It is the source of a bipolar molecular outflow with length $\ell = 0.11$ pc and dynamical age $\Delta t \sim 10^4$ yr (e.g. Hsieh et al. 2017, Barsony et al. 2010). I16253's mid-infrared spectrum contains many spectral lines of OH, which are bright compared to those of the species which usually dominate the spectra of YSOs. In the following we show that water surrounding I16253 is photodissociated by protostellar UV into OH and atomic hydrogen. At I16253's mass and luminosity, the necessary UV emission must arise in disk-star accretion flows.

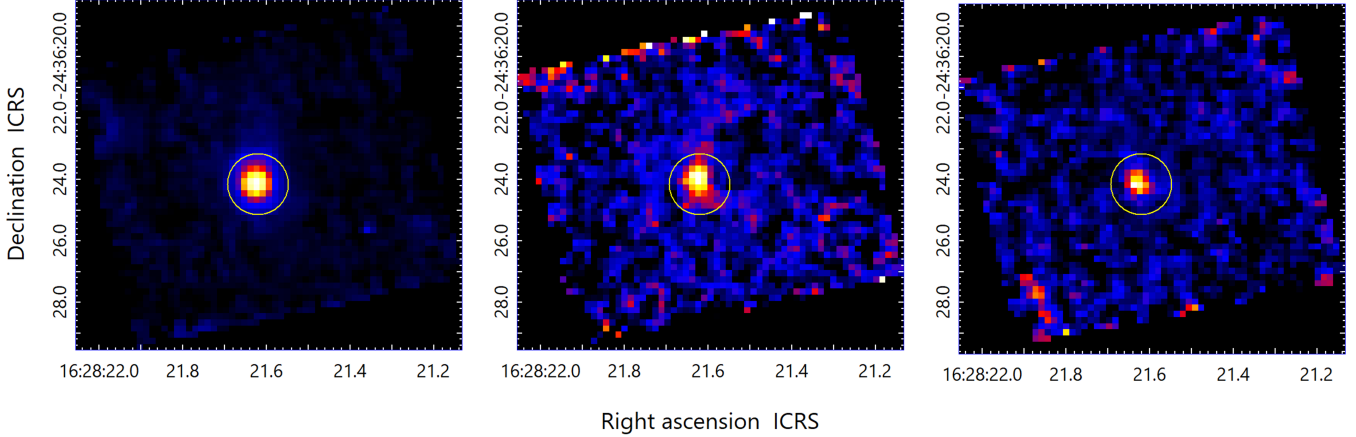


Figure 1. Images of the central object in IRAS 16253-2429. From left: $\lambda = 14 \mu\text{m}$ continuum, arcsinh stretch; $\text{CO}_2 01^1-00^0$ Q branch, $\lambda = 14.98 \mu\text{m}$, linear stretch; and OH X1.5 $N = 16$ A' , $\lambda = 16.84 \mu\text{m}$, linear stretch. Brightness limits are -1σ (black) to peak intensity (white) in each case. The yellow circle is the 1 arcsec radius extraction aperture for the measurements listed in Table 2, and is centered on ICRS coordinates $\alpha = 16:28:21.60$, $\delta = -24:36:23.4$ (Hsieh et al. 2017).

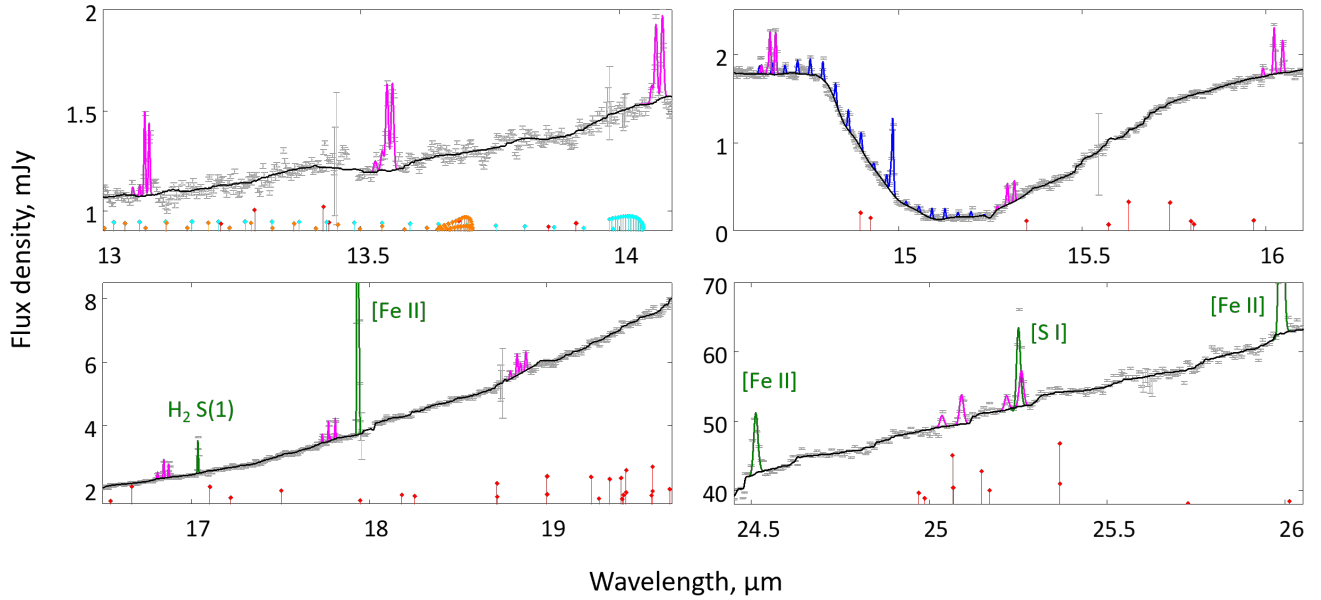


Figure 2. Representative sections of the JWST-MIRI spectrum of I16253, shown as gray points and errorbars. The latter include propagated noise and flux-calibration uncertainty. The continuum fit is overlaid in black, along with fits of the MIRI spectral point-spread function to emission lines of OH (pink), CO_2 (blue), and assorted H_2 and atomic or ionic lines associated with the protostar’s outflow: collimated jet or wider-angle wind, or cavity wall (green). Marked along the bottom of each frame are lines not detected: H_2O in red, HCN in cyan, and C_2H_2 in orange. They are plotted with notional flux densities, in the vertical scale of their frame and measured from the wavelength axis. These flux densities are calculated from the relative abundances and excitation temperatures found for these molecules in the Class II YSO GW Lup by Grant et al. (2023), which we use only as an example of a spectrum containing the complete cast of strong mid-infrared lines from YSOs. The number of CO_2 molecules we detect is an order of magnitude larger than detected in GW Lup, but the temperature we find for them ($T = 110 \text{ K}$) is substantially smaller than GW Lup’s $T = 400 \text{ K}$ (Section 5.3).

3. OBSERVATIONS AND DATA REDUCTION

We observed I16253 on 2022 July 22-23, as part of the James Webb Space Telescope (JWST) General Observing Program 1802 (*Investigating Protostellar Accretion* [IPA]; S.T. Megeath, PI). We used the JWST Mid-Infrared Instrument (MIRI) Medium-Resolution Spectrograph (MRS) integral-field-unit (IFU), to obtain spectral images at wavelengths $\lambda = 4.9 - 27 \mu\text{m}$ of $6 \text{ arcsec} \times 6 \text{ arcsec}$ to $9 \text{ arcsec} \times 9 \text{ arcsec}$ fields centered on the protostar. The spectral images were comprised of 2×2 mosaics of individual IFU frames with at least 10% overlap, each observed with four-point dithers. The MIRI MRS IFU pixel scale is $0.27 \times 0.27 \text{ arcsec}^2$ at its longest wavelengths and $0.2 \times 0.2 \text{ arcsec}^2$ at its shortest. Thus the diffraction-limited point spread function, of diameter $1 \text{ arcsec} \times \lambda/27 \mu\text{m}$, is well sampled by MIRI's IFU for $\lambda \gtrsim 10 \mu\text{m}$. We used all twelve MIRI MRS spectral sub-bands, obtaining resolving power ranging over $\lambda/\Delta\lambda = 1350 - 3700$ as wavelength ranges over $\lambda = 27 - 4.9 \mu\text{m}$. More details of our observations are given by Narang et al. (2024), Rubinstein et al. (2024), and Federman et al. (2024).

4. DATA ANALYSIS

Coincident with the protostellar position in our data cubes is an unresolved (FWHM $< 80 \text{ AU}$ diameter) source of spectral lines and continuum at $\lambda \geq 10 \mu\text{m}$, shown in Figure 1. We chose an aperture with radius 1 arcsecond, large enough to encompass this source at the longest MIRI wavelengths. Within this aperture we extracted the flux density F_ν at $\lambda = 4.9 - 27 \mu\text{m}$ from the data cubes. We masked wavelengths at and around those of spectral lines we detected; fit the remaining baseline, smoothed over 51 channels to a cubic spline; subtracted this baseline from the data; and simultaneously fit Gaussian profiles with the instrumental-resolution width to the baseline-subtracted data at the wavelengths of each spectral line. For ionic, atomic, and H₂ lines, which arise in I16253's high-speed jet or wider-angle wind, (Narang et al. 2024), we included several velocity components to ensure capture of all the flux. All other lines we detect are spectrally unresolved and consistent with the protostar's systemic radial velocity. Table 2 is a list of the emission lines we detect, and upper limits for the OH pure rotational lines we do not. In Figure 2 we show example segments of the extracted spectrum.

I16253's mid-infrared emission-line spectrum is dominated by lines of OH and gas-phase CO₂. We detect every pure rotational transition of OH in the $\lambda = 10 - 27 \mu\text{m}$ range: both of the $X^2\Pi_{3/2}$ and $X^2\Pi_{1/2}$ electronic configurations (henceforth X1.5 and X0.5); lower-state

rotational quantum numbers $N = 10 - 33$; and generally both A-doublet components A'' and A' resolved from one another, as in Figures 2 and 3.

We also detect the P, Q, and R branches (respectively $\Delta J = +1, 0, -1$) of the fundamental, $\nu_1\nu_2^\ell\nu_3 = 01^10 - 00^00$ rotation-vibration band of CO₂. The rotational structure of the Q branch is spectrally unresolved, but the P and R branches are distinct, and the latter is detected through R(16) (i.e. $J = 17 - 16$). In Appendix A we briefly summarize the mid-infrared spectroscopy of OH and CO₂, and define the terms we use here. The unresolved nature of I16253's OH and CO₂ emission (Figure 1) suggests that it arises near ($< 40 \text{ AU}$) the central protostar.

This collection of lines is unlike those of most low-mass YSOs, Class 0/I (van Gelder et al. 2024a) or Class II (e.g. Pontoppidan et al. 2010, Carr & Najita 2011). We do not detect several molecular species whose lines usually dominate the mid-infrared spectra of protoplanetary disks, notably H₂O, HCN, and C₂H₂. Upper limits on $\lambda = 10 - 27 \mu\text{m}$ lines of these species are much smaller than those of the detected OH and CO₂ lines. Most Class 0/I objects observed so far display lines of both H₂O and CO₂, with the former brighter than the latter (van Gelder et al. 2024a). In Figure 2 we mark the lines of these undetected molecules and indicate their relative strength in a Class II YSO spectrum which contains all these molecular spectra. In I16253 we also do not detect vibrationally-excited OH, higher-energy ro-vibrational modes of CO₂, or rotational transitions between the OH X1.5 and X0.5 ladders.

I16253's $\lambda = 15 \mu\text{m}$ CO₂ ice absorption feature turns out to yield useful constraints on the nature of the OH and CO₂ line emission. We show a line-subtracted spectrum of the ice feature's optical depth τ in Figure 4. Its shape is similar to that toward many other Class 0/I objects which have been modeled as cold ($T \lesssim 35 \text{ K}$) icy grains along the line of sight through the protostar's envelope (e.g. Pontoppidan et al. (2008), Zasowski et al. (2009)); it is similar to the ice feature recently observed toward the edge-on Class 0 object Ced 110 IRS4A (Rocha et al. 2025), to which the embedded disk probably makes significant contributions. It lacks very prominent segregated-CO₂ features at $\lambda = 15.1$ and $15.25 \mu\text{m}$, as in objects which have warmer ($> 80\text{K}$) ices (Brunkens et al. 2025). We modeled the absorption with cold ($T = 10 \text{ K}$), small ($a \ll \lambda$) grains of a continuous distribution of ellipsoidal shapes (CDE; Bohren & Huffman (1998), equation 12.36), using optical constants in

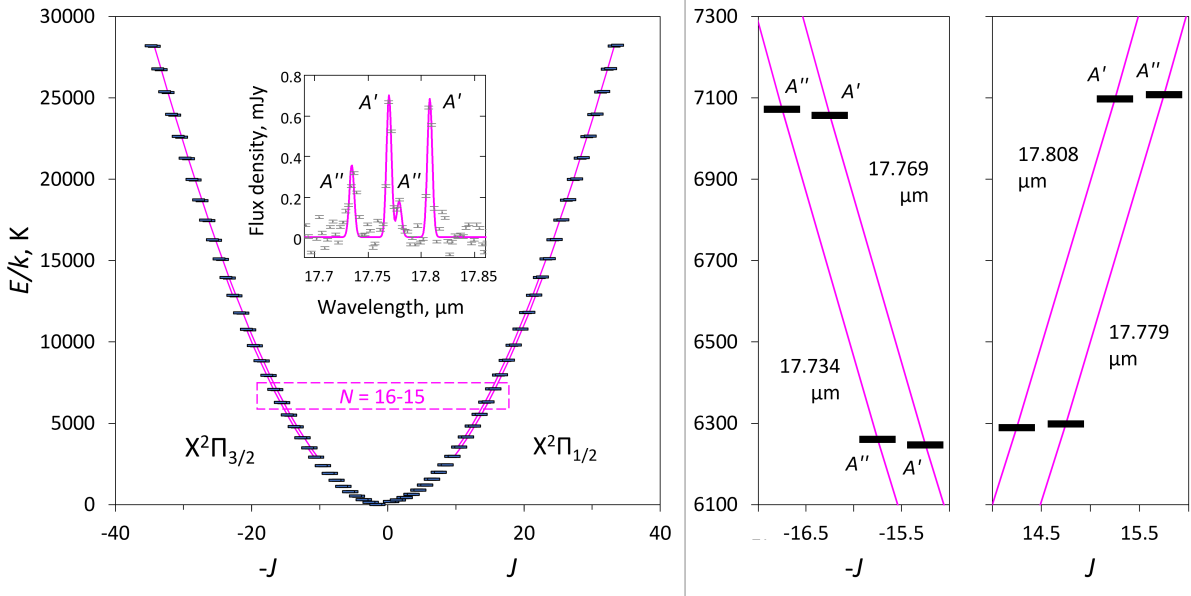


Figure 3. Energy level diagram of the lowest-energy $v = 0$ states of OH. Left: rotational states of the ground electronic configuration, with fine structure and Λ -doubling shown, and detected transitions indicated with pink lines. Inset: example MIRI spectrum of the $N = 16-15$ transitions. Right: zoom in to the states involved in the $N = 16-15$ transitions. For clarity, the Λ -doublet A'' and A' states are each plotted with symmetrical displacement about their total angular momentum quantum number J . Comparison of the inset spectrum and the zoomed view illustrates the faintness of the A'' lines relative to the A' transitions, a common feature of the OH lines in Figure 2.

the Leiden Ice Database for Astrophysics³⁵, and CDE grain absorbance from Rocha et al. (2025) and Pontoppidan et al. (2008). From the fitted components we computed molecular column densities \mathcal{N} ,

$$\mathcal{N} = \frac{1}{A_b} \int \tau d\nu , \quad (1)$$

and took the band strength A_b to be 1.1×10^{-17} cm molecule $^{-1}$ (Pontoppidan et al. 2008). The resulting minimum- χ^2 fit, shown in Figure 4, is similar to the spectral decomposition of Ced 110 IRS4A by Rocha et al. (2025). We find a column density ratio $\mathcal{N}(\text{H}_2\text{O})/\mathcal{N}(\text{CO}_2) = 1.9 \pm 0.7$, placing the object along one edge of the distribution of this ratio in the survey by Pontoppidan et al. (2008), but not discordant with the population. We will assume, below (section 5.2), that all significant components of ice in this young protostar have this same value of $\mathcal{N}(\text{H}_2\text{O})/\mathcal{N}(\text{CO}_2)$, though because a relatively narrow selection of optical constants was used, and the ratio is expected to vary from place to place within I16253, we will not propagate the fitting uncertainties in the calculations below.

5. RESULTS

5.1. I16253's OH emission is fluorescence driven by accretion-generated UV

I16253's OH emission is predominantly from lines between the lower-energy, A' members of Λ -doublets, equally bright in the X1.5 and X0.5 configurations. The A'' lines are much fainter, especially for larger values of N . This is apparent in Figures 2 and 3, and in the flux ratios for the full range of N as plotted in Figure 5. However, the radiative decay rates (Einstein A coefficients) of A'' and A' states are practically the same, for a given N (Brooke et al. 2016, Noll et al. 2020)³⁶. Taken together with the small A''/A' flux ratios, this requires all the OH lines to be optically thin, with flux directly proportional to the number of upper-state molecules. Thus the populations of the Λ -doublet states are strongly anti-inverted. This condition cannot be produced or significantly modified by collisional processes. Collisional de-excitation rates have not been calculated for OH rotational states in the present range, but those at smaller N (Offer et al. 1994, Kalugina et al. 2014) suggest that collisions would lead to A'' and A' state populations closely similar to one another.

³⁶ See <https://hitran.org/>.

³⁵ See <https://icedb.strw.leidenuniv.nl/>.

Photodissociation of H₂O by photons in water's second absorption band (SAB) at $\lambda = 114 - 145$ nm efficiently produces OH with properties precisely replicating our observations. In laboratory measurements and simulations alike (Mordaunt et al. 1994, Dixon 1995, Harich et al. 2000, Zhou et al. 2015, Young et al. 2018, Chang et al. 2019), $\lambda = 121.6$ nm photodissociation of H₂O produces OH with low electronic and vibrational excitation: about 82% in X1.5 and X0.5, in equal numbers, and 75% in $v = 0$. The products have high rotational excitation, $N = 30 - 45$. If the target H₂O is rotationally cold ($T \lesssim 200$ K), a large fraction of the OH is produced with $A''/A' \ll 1$, and with $A''/A' \rightarrow 0$ as $T \rightarrow 0$ (Dixon 1995).

As these OH molecules are produced with large values of N , whether in the ground electronic and vibrational manifolds or not, they decay rapidly to other large- N states of $X^2\Pi$ $v = 0$. From there, they decay down the rotational ladders of X1.5 and X0.5. All the states have small lifetimes, 0.001-0.01 sec for $N = 10 - 33$, and the molecules reach the lower ($N < 10$) rotational states before they are themselves dissociated by protostellar UV ($> 10^4$ sec; Section 5.2). Thus the steady-state populations of the OH rotational states are given in terms of the state populations and their A coefficients as

$$n_{J+1}A_{J+1,J} = n_JA_{J,J-1} \quad , \quad (2)$$

each term obtained from an OH rotational line flux. The sum of the four values of $n_JA_{J,J-1}$ which belong to orbital angular momentum state N is $\dot{n}_f(N)$, the rate in photons sec⁻¹ at which OH molecules pass through the fluorescent cascade. According to Equation 2, $\dot{n}_f(N)$ is independent of N in a steady state.

The OH Λ -doublets have anti-inverted populations in all the rotational states we observe. However, A''/A' increases as N decreases, reaching $A''/A' = 0.4 - 0.5$ at $N \lesssim 15$ (Figure 5). This may indicate contribution to the OH spectrum in this range by processes besides fluorescence, as we address below.

A small number of previous YSO-related observations reveal prominence of OH emission over H₂O emission similar to our spectra. Tappe et al. (2008), Tappe et al. (2012), and Tabone et al. (2021) invoked SAB photodissociation of H₂O in their account of OH spectra of terminal shocks in YSO outflows. So did Neufeld et al. (2024), with JWST-MIRI spectra of HOPS 370's jet. The mid-infrared line spectrum of the Class II YSO TW Hya is similar to that of I16253; Najita et al. (2010) invoked SAB photodissociation of H₂O and prompt emission by OH to explain the OH emission. Carr & Najita (2011) and Carr & Najita (2014) ascribed the OH emission from the Class I/II YSO DG Tau in part to SAB

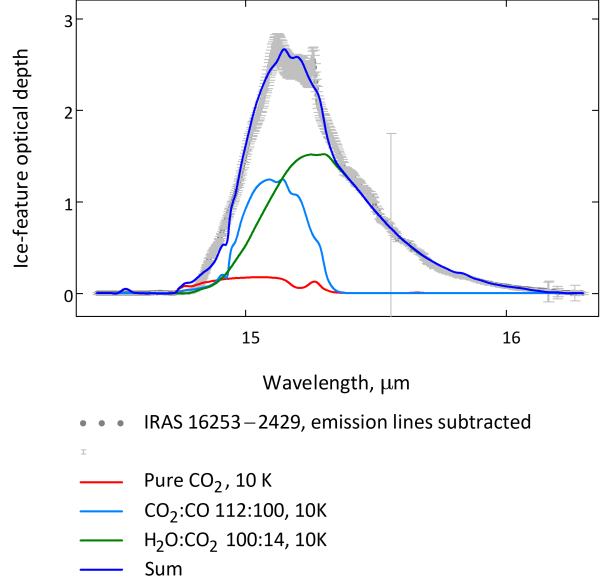


Figure 4. Optical depth spectrum of the CO₂ ice absorption feature. Overlaid on the JWST data (gray points and errorbars) is the best fit found for small ($\ll 15$ μm) grains of CDE shape distribution, coated with cold ($T = 10$ K) ice analogues: CO₂ : CO from Pontoppidan et al. (2008) and Rocha et al. (2025), H₂O : CO₂ and pure CO₂ from Ehrenfreund et al. (1997). This ice mixture has column density ratio $\mathcal{N}(\text{H}_2\text{O})/\mathcal{N}(\text{CO}_2) = 1.9$.

photodissociation of H₂O followed by OH rotational-line fluorescence. Recently the Class II YSO CX Tau was also suggested to have UV-excited fluorescent OH rotational emission (Vlasblom et al. 2025). Zannese et al. (2024) invoked photodissociation to explain the OH emission from externally-illuminated protoplanetary disks adjacent to the Orion Nebula. In solar-system comets, Bonev & Mumma (2006) observed OH population ratios in $v = 1$, $N = 16$ similar to those we see in the same rotational states of $v = 0$ (Table 2). They suggested SAB photodissociation products as the origin, among other possibilities.

Three alternatives to OH production by SAB dissociation of H₂O are not supported by our observations: H₂O photodissociation in H₂O's first absorption band (FAB; $\lambda = 145 - 186$ nm); OH production by O – H₂ reaction; and collisional and radiative excitation by warm gas and/or the protostar's infrared continuum emission:

- H₂O photodissociation in the FAB leads to OH predominantly in the X1.5 and X0.5 configurations, but in $v \geq 1$ vibrational states and $N \lesssim 5$ rotational states, and with Λ -doublet populations inverted: $A''/A' > 1$ (e.g. Andresen et al. 1984): the diametric opposite of our observations. In

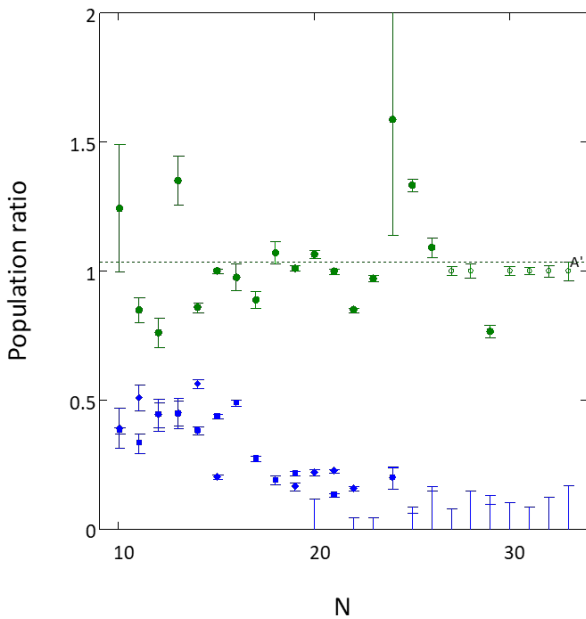


Figure 5. OH rotational-state population ratios: X1.5 A''/A' (blue squares), X0.5 A''/A' (blue diamonds), and X0.5 $A'/X1.5 A'$ (green circles), all as functions of the lower-state orbital angular momentum quantum number N . As these ratios are extremely insensitive to extinction, they are plotted without extinction correction. The open green circles at $N = 27$ – 28 and 30 – 33 represent spectrally-unresolved combinations of X0.5 $A'/X1.5 A'$ lines, plotted with notional ratios of unity merely to show their propagated uncertainties. The upper limits at $N = 27$ – 28 and 30 – 33 account for both A''/A' ratios and the unresolved $A' – A'$ pair. The dashed green line marks the mean value of the solid green points, 1.04 ± 0.21 .

obedience to the selection rules, OH produced in this manner decays rapidly to small- N rotational states within the $v = 0$ vibrational manifold, skipping over the states probed by our measurements.

- $O(^1D) + H_2 \rightarrow H + OH$ also produces OH in the $X^2\Pi$ configurations, and with a wide range of rotational states populated, but also with $v \geq 1$ vibrational manifolds populated similarly to $v = 0$ (Liu et al. 2000, Alexander et al. 2004). This would produce many vibrationally-excited OH lines in our spectrum similar in flux to the pure rotational lines (Tabone et al. 2021), which we do not detect. The reaction does, however, produce $A''/A' < 1$ in the range we see, at $N \leq 15$ (Alexander et al. 2004, Tabone et al. 2024). Judging from the excitation and output spectrum in the Tabone et al. results, and provided that sufficient $O(^1D)$ is present, this mechanism may contribute to the rise in A''/A'

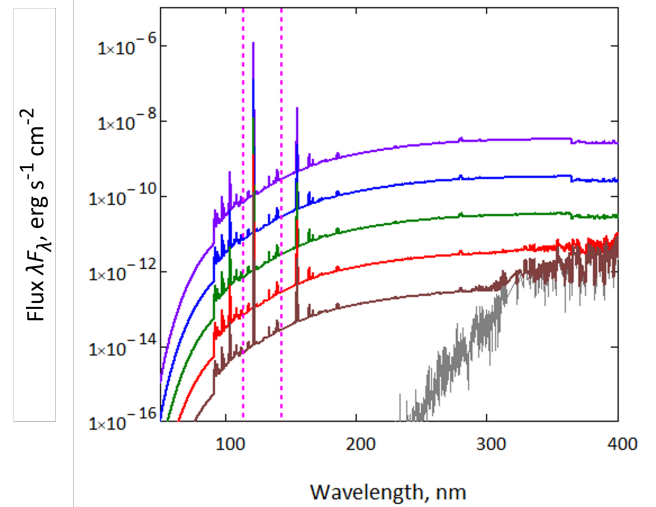


Figure 6. Flux λF_λ at distance $d = 140$ pc, as a function of wavelength, for the small grid of accretion models described in Section 5.2. The underlying stellar spectrum is plotted in gray. Stellar plus pre- and post-shock accretion-powered flux is plotted for accretion rates $\dot{M} = 10^{-6}$ (uppermost, purple), 10^{-7} (blue), 10^{-8} (green), 10^{-9} (red), and $10^{-10} M_\odot$ year $^{-1}$ (brown, lowest). Dashed pink lines mark the edges of water's second absorption band (SAB).

and OH rotational line flux we see at the smaller values of N .

- As mentioned above, collisional excitation cannot produce small A''/A' . Nor can infrared radiative pumping: because the Einstein A coefficients are practically the same for a given N , so are the Einstein B coefficients, and the Λ doublets are too closely spaced for a broadband source of radiation to select one Λ -doublet state over the other.

5.2. Accretion-generated UV from low-mass protostars

Low-mass protostars like I16253 only produce significant UV radiation *via* accretion. The main alternative would be strong shocks within the protostar's high-speed jet. However, the shocks in I16253's jet are relatively slow ($v_s \lesssim 55$ km sec $^{-1}$; Narang et al. 2024), incapable of generating substantial UV (compare Neufeld et al. (2024)). Shocks within the jet also occupy a small solid angle in the view of the circum-protostellar regions. We conclude that the UV responsible for OH production is generated by accretion processes around the protostar.

To relate the extinction-corrected OH fluorescence rate $\langle \dot{n}_f \rangle$ to the disk-star accretion rate \dot{M}_a , we have created a small grid of model of far-UV, $\lambda = 50$ nm – 400 nm, spectra (Figure 6). The underlying stellar spectrum is that of a Phoenix model photosphere (Husser et al. 2013) for a star with mass $M = 0.15 M_\odot$, radius $R = 1.3 R_\odot$, and effective temperature $T_e = 3200$ K at

distance $d_0 = 140$ pc. The model grid covers accretion rates $\dot{M}_a = 10^{-10} - 10^{-6} M_\odot \text{ year}^{-1}$. UV continuum and line emission is shock-excited on the stellar surface by material falling from the circum-protostellar disk's inner radius at $R_x = 3.5 R$. Emission from the post-shock material is calculated according to Pittman et al. (2022), using the methods of Calvet & Gullbring (1998) and Robinson & Espaillat (2019).

To this we add observations of line emission not represented in the accretion-shock models, and thought to be produced by gas in the star's magnetospheric accretion funnel (Muzerolle et al. 2001). The brightest of these lines, H I Ly α $\lambda = 121.6$ nm, lies within the SAB. In a sample of 16 accreting stars, France et al. (2014) found that Ly α flux is proportional to, and 10.5 ± 6.6 times larger than, the integrated $\lambda = 91.2 - 165$ nm continuum. We added this continuum-scaled line emission to the accretion models, resulting in the model spectra shown in Figure 6. The total accretion-related luminosity of the models is $L_{acc} = 3.0 \times 10^{-3} L_\odot \times (\dot{M}_a/10^{-9} M_\odot \text{ year}^{-1})$.

5.3. Extinction-corrected parameters of hydroxyl and carbon dioxide

From our spectra we can obtain extinction-corrected values of the OH fluorescence rate \dot{n}_f , and the number and temperature of CO₂ molecules, n_{CO_2} and T . Our observations offer two independent measurements of reddening. First is the set of OH emission lines, for which each rotational transition in the fluorescent cascade has the same total photon flux. We calculate wavelength-dependent reddening by ratio of OH photon flux $\dot{n}_f(N)$ to its average value over a range of N , $\langle \dot{n}_f \rangle$; that is, departure from a uniform value of $\dot{n}_f(N)$ can be ascribed to extinction. To ensure the exclusion of OH emission from mechanisms besides that from the fluorescent cascade, we use only the lines with $N \geq 17$. This range spans a substantial portion of the broad silicate- and water-ice-related extinction evident in Figure 2.

Second is the set of CO₂ emission lines, which we assume to arise in the same material as the OH lines. Like OH, these lines appear to be optically thin: even if the emission source were less than a few AU in radius and the lines were only thermally broadened, they would have peak optical depth $\tau \lesssim 10^{-3}$. We lack accurate excitation rate coefficients for CO₂ – H₂ collisions with which to model the populations of CO₂'s states, so we assume a local thermal equilibrium (LTE) distribution at temperature T . This leads to an acceptable account of the spectrum, as shown in Figure 7. We also show in Appendix B.1 that the LTE approximation is reasonable, and that it gives the number of CO₂ molecules

accurately; in other words, that optical pumping (van Gelder et al. 2024a) is negligible compared to collisions in populating the upper states of the detected lines.

The CO₂ flux ratios determine the reddening within the CO₂ ice feature. Combined with a suitable extinction model, either or both of the OH and CO₂ measurements leads to a total extinction determination. We include both ³⁷ in a χ^2 -minimization fitting procedure, using as free parameters the average OH photon flux $\langle \dot{n}_f \rangle$ in the fluorescent cascade; the temperature T and total number of CO₂ molecules n_{CO_2} ; and the column density \mathcal{N}_{ext} of extinguishing material, assumed to be a nonemitting foreground screen. As in Narang et al. (2024), we adopt the KP5 extinction model (Pontoppidan et al. 2024). KP5 has been constructed from optical properties of icy dust grains and constrained by infrared and submillimeter extinction measurements in dense molecular clouds (Chapman et al. 2009, Shirley et al. 2011). KP5 incorporates a different ice mixture and temperature ($\mathcal{N}(H_2O)/\mathcal{N}(CO_2) = 5$, $T = 20 K$) than we found to be a good match for the I16253 CO₂ ice feature. However, the shapes of the two mixtures' ice features (Ehrenfreund et al. 1999) are similar, particularly along their short wavelength edge where the strongest CO₂ emission-line constraints lie, in the form of the CO₂ R branch. To adapt KP5 to the mixture we infer would make negligible difference in the extinction result. Results of the fit and extinction correction appear in Figure 7 and Table 1. Our derived value of visual extinction, 26.7 ± 3.0 mag, agrees well with that derived from H₂ emission within our aperture, but associated with I16253's jet or wider-angle outflow: $A_V = 26.5 \pm 0.5$ mag (Narang et al. 2024). Under the assumption that extinction between central star and molecules is negligible, radiative equilibrium determines a typical stellocentric distance $r = 2.5$ AU for the gas-phase CO₂.

5.4. Mass accretion rate of I16253

The mass accretion rate \dot{M}_a responsible for the H₂O-dissociating UV is determined by \dot{n}_f and λF_λ , calculated above, and the steady-state number of water molecules exposed to protostellar UV, n_{H_2O} . We do not detect this H₂O, but it is necessarily located with the emitting OH, and therefore with the CO₂. In the envelope of I16253, where H₂O and CO₂ are largely frozen into grains, we found above that $\mathcal{N}(H_2O)/\mathcal{N}(CO_2) = 1.9$ (Section 4) along the sightline toward the central protostar. This icy dust is representative of the original ingredients of the warmer central structures of I16253. Thermal and chemical processes could have modified the

³⁷ “Either” instead of “both” leads to two closely similar results.

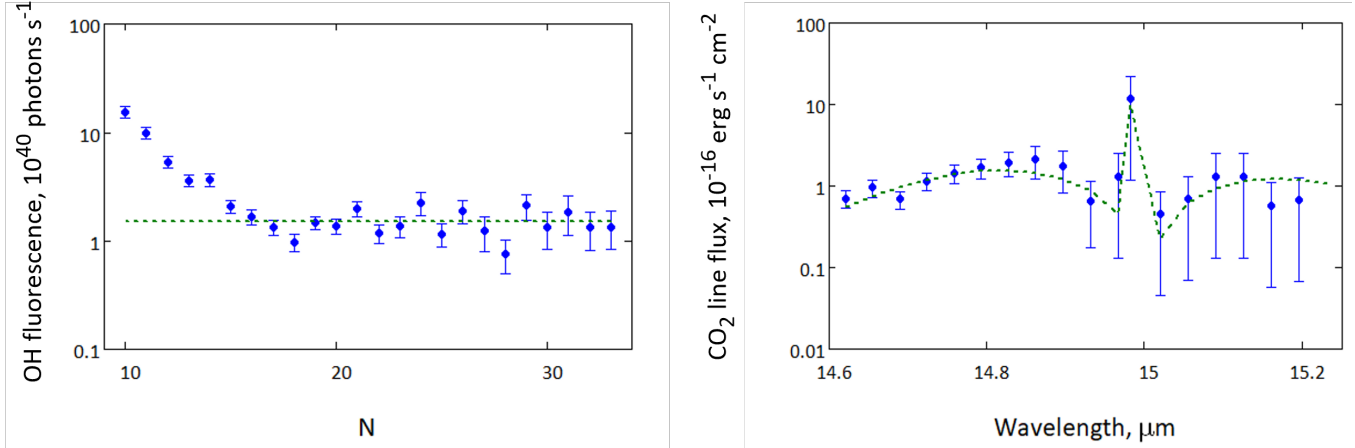


Figure 7. Left: extinction-corrected OH-line fluorescence luminosity per rotational transition, $\dot{n}_f(N)$. The dashed line indicates the extinction-corrected $\dot{n}_f(N)$ averaged over the range $N \geq 17$, from Table 1. Right: extinction-corrected CO_2 -line flux. The dashed curve is the fitted emission for n_{CO_2} and T given in Table 1. Uncertainties in the plot are dominated by those propagated from the extinction correction, and are particularly large near the center of the CO_2 ice feature.

Table 1. Extinction-correction fit to OH and CO_2 line fluxes

Extinction column density, \mathcal{N}_{ext}	$(7.3 \pm 0.8) \times 10^{22}$	H atoms cm^{-2}
Visual extinction, A_V	26.7 ± 3.0	mag
Fluorescent OH luminosity per rotational transition, $\langle \dot{n}_f \rangle$	$(1.5 \pm 0.6) \times 10^{40}$	photons s^{-1}
CO_2 gas, n_{CO_2}	$(1.6 \pm 0.5) \times 10^{44}$	molecules
CO_2 gas temperature, T	110.0 ± 3.6	K
Reduced χ^2	1.1	

relative abundances considerably in the inner parts of I16253, but such changes are not currently constrained by observations. In anticipation of future detection of H_2O emission from I16253, or chemical modelling beyond the scope of this article, we assume, consistent with our observations, that the OH-parental H_2O follows the CO_2 at the relative abundance observed in the CO_2 ice feature, and we show in Appendices B.1 and B.2 that this assumption is plausible.

To obtain \dot{M}_a , we consider three scenarios: one, i , in which the H_2O -dissociating photons exhaust the supply of water; and two others, ii and iii , in which the H_2O -dissociating photons are outnumbered by water molecules. The latter scenarios differ in the state of the reservoir of CO_2 and H_2O : gas phase or solid phase.

Scenario i. The central star's UV photon luminosity in the SAB, capable of dissociating water into OH molecules in the states we see, is $\dot{n}_{SAB} = \frac{4\pi d_0^2}{hc} \int_{SAB} \lambda F_\lambda(\lambda) d\lambda$. All of our accretion models (section 5.2) turn out to have $\dot{M}_{model}/\dot{n}_{SAB,model} = 3.2 \times 10^{-25}$ gm. If the observed OH fluorescence rate $\langle \dot{n}_f \rangle$

equals or exceeds the rate at which H_2O molecules are provided, then \dot{n}_{SAB} is no smaller than $\langle \dot{n}_f \rangle$:

$$\dot{M}_a(i) = \langle \dot{n}_f \rangle \dot{M}_{model}/\dot{n}_{SAB,model} > 4.2 \times 10^{-11} M_\odot \text{ year}^{-1} , \quad (3)$$

at 95% confidence.

Scenario ii. Take the parent H_2O to be gas-phase molecules belonging to one of the fluid components of the central star's surroundings, with its chemical populations in steady state, and lying where the starlight heating of dust matches the temperature determined for CO_2 (Section 5.3). Possible locations are the innermost outflow-cavity wall, as in a protostellar hot core; in the innermost part of I16253's jet; or interior to the ice line in the embedded disk. In the latter two locations it would intercept a relatively small fraction of the stellar UV, while the hot core would cover most of the central star's sky. In Appendix B.1 we assume such a hot core to exist, and calculate n_{H_2O} , obtaining

$$n_{\text{H}_2\text{O}}(ii) = (3.0 \pm 1.0) \times 10^{44} \text{ molecules} . \quad (4)$$

For $T = 110$ K, none of the $\lambda = 5 - 27 \mu\text{m}$ emission lines of this H_2O population would lie above the noise in our observations.

Scenario iii. Take icy solids — dust grains or larger bodies — to be the reservoir of H_2O and CO_2 . The molecules would be photodesorbed into the gas phase and then photolyzed, in the manner of solar-system comets and their comae (e.g. Crovisier 1989). These grains could lie anywhere within UV range of the star, including the outflow cavity or disk atmosphere as well as the cavity walls. In Appendix B.1 we correct for the differences in desorption and subsequent photolysis between H_2O and CO_2 , thereby obtaining

$$n_{\text{H}_2\text{O}}(iii) = (5.1 \pm 1.9) \times 10^{44} \text{ molecules} . \quad (5)$$

OH in the states we detect is produced at the rate $\dot{n}_{\text{OH}}(F_\lambda) = n_{\text{H}_2\text{O}} Q(\sigma_{\text{SAB}}, F_\lambda)$, where Q is the photolysis rate of gas-phase H_2O (see Appendix B.2). \dot{n}_{OH} depends upon the accretion rate M_a through F_λ ; M_a is determined by equality of \dot{n}_{OH} to the observed OH fluorescence rate $\langle \dot{n}_f \rangle$. We calculated \dot{n}_{OH} for our grid of accretion models, and interpolated among the results to find $\dot{n}_{\text{OH}} = \langle \dot{n}_f \rangle$. Thereby our two estimates of $n_{\text{H}_2\text{O}}$ lead to

$$\begin{aligned} \dot{M}_a(ii) &= (4.1 \pm 2.9) \times 10^{-10} M_\odot \text{ year}^{-1} \\ \dot{M}_a(iii) &= (2.5 \pm 1.7) \times 10^{-10} M_\odot \text{ year}^{-1} \\ \dot{M}_a(\text{adopted}) &= (3.3 \pm 2.2) \times 10^{-10} M_\odot \text{ year}^{-1} , \end{aligned} \quad (6)$$

where the adopted value is the average of the other two, and all are consistent with Equation 3. A linear combination of the scenarios *ii* and *iii* would also be plausible, and would perforce give a result similar to Equation 6. All these accretion rate estimates are vastly less than that inferred for I16253 10⁴ years ago, when its now-0.1-pc-long bipolar molecular outflow began to form: $\dot{M}_a \approx 5 \times 10^{-7} M_\odot \text{ year}^{-1}$ (Hsieh et al. 2017).

6. DISCUSSION

Equations 6 formally give lower limits to \dot{M}_a . Some of the SAB photons may be absorbed on their way to the H_2O , by dust or other molecules. Neither of the locations posited for the OH-parental population are guaranteed to fill the central star's sky, so UV photons may also escape to larger radii. We can note, however, that suitable absorbing material is seen to be distributed all

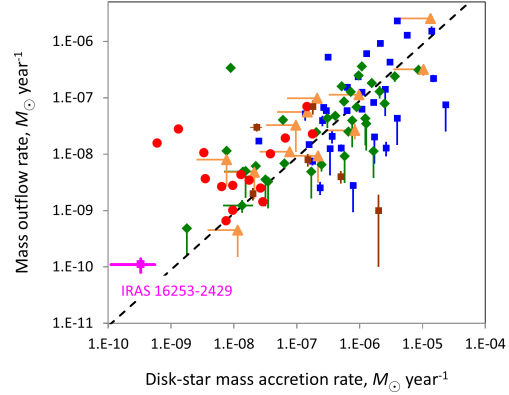


Figure 8. Accretion and outflow rates, \dot{M}_a and \dot{M}_w , for I16253 (present work, pink square) overlain on accretion and outflow rates from a survey by Watson et al. (2016) of Class 0/I/flat-spectrum protostars (blue squares, green diamonds, and orange triangles, respectively); of low-mass Class 0 protostars and proto-brown dwarfs (Riaz & Bally 2021, brown squares); and of selected Class II YSOs (Hartigan et al. 1995, Gullbring et al. 1998; red circles). The dashed line marks $\dot{M}_w = 0.1 \dot{M}_a$.

around the central star in projection (Federman et al. 2023, Federman et al. 2024, Rubinstein et al. 2024). Certainly a large fraction of the sky seen from the central star is filled with nearby icy solids which would fit in scenario *iii*. The absorbing material that produces the CO_2 ice feature (Section 4) lies far from the disk/envelope midplane as seen from the star. I16253's disk axis is inclined 64.1° from the plane of our sky (Aso et al. 2023); our line of sight has “declination” 25.9° in I16253's sky. Accordingly, 44% of the protostar's sky lies at smaller “declination” than we do, along which directions the protostar's UV would encounter material in an even better position to absorb H_2O -dissociating UV than that directly along our line of sight. We conclude that the resulting value of $\dot{M}_a(iii)$ accounts for a large fraction of the accretion-related UV, and that the actual accretion rate cannot be much larger than that given in Equations 6.

Occupying a much smaller portion of the protostar's sky, I16253's embedded disk intercepts far less of the dissociating UV than would the H_2O reservoirs of scenarios *ii* and *iii*. A Class II YSO, lacking these additional reservoirs, would not produce OH line emission as prominently as I16253, relative to H_2O emission. This agrees with observations (e.g. Figure 2). As for the Class II YSOs with exceptional OH emission which we list in Section 5.1: DG Tau has a residual envelope which is massive by Class II standards, evident in extended, scattered visible light (Stapelfeldt et al. 1997) and a flat mid-IR to submillimeter spectral energy distribution

(Ohashi et al. 2023). That some of this material covers large portions of the central star’s sky is evident in the starlight’s large visible polarization (Bastien 1982): much of the detected starlight has been scattered, despite the small angle between DG Tau’s disk axis and our line of sight (Ohashi et al. 2023). Thus DG Tau very probably has a reservoir of H₂O with distribution similar to I16253’s. We can only speculate that TW Hya’s exceptional OH emission is related to the structure of its transitional disk (e.g. Menu et al. 2014).

In Figure 8 we show I16253’s mass accretion rate in the context of other, mostly larger-mass or larger-luminosity protostars. I16253 has a high-speed jet, appearing in the ionic and atomic lines, which dominates mass loss from the central few tens of AU, and from which Narang et al. (2024) infer mass flow rate $\dot{M}_w = (1.1 \pm 0.3) \times 10^{-10} M_\odot \text{ year}^{-1}$. This, plus the present result, place I16253 well within the outflow-accretion trend for YSOs, and close to the canonical $\dot{M}_w \sim 0.1 \dot{M}_a$ of magnetocentrifugally-accelerated outflows (e.g. Pelletier & Pudritz 1992). As Narang et al. (2024) show, I16253’s jet is highly collimated (opening angle $\lesssim 3^\circ$), requiring that the jet and accretion disk are strongly linked. Thus the small values of \dot{M}_a and \dot{M}_w do not suggest an unusual arrangement for the footpoints of the magnetic field which accelerates I16253’s outflow.

I16253’s luminosity, $L_{bol} = 0.16 L_\odot$, is dominated by intrinsic luminosity, with only a 1% contribution by accretion: $L_{acc} = 1.6 \times 10^{-3} L_\odot$. By its mass ($M = 0.15 M_\odot$) and intrinsic luminosity, I16253’s central star lies close to the stellar mass-luminosity birthline estimated by Hartmann et al. (2025), as do several other Class 0/I systems with measured stellar masses (Hartmann et al. 2025). Coupled with the large mass of its infalling envelope, these properties show that I16253 is certainly an early-stage protostar, with an age well within the ~ 0.5 Myr span during which protostars accrete most of their mass (e.g. Dunham et al. 2014, Fischer et al. 2017, Federman et al. 2023). In I16253 we measure much smaller accretion and outflow rates than those typically reported in protostars, as is clear in Figure 8, and apparently than those of I16253 itself some 10^4 years ago. At I16253’s current accretion rate it would have taken about $M/\dot{M}_a = 450$ Myr to accumulate its current mass (see also Narang et al. 2024). This is qualitatively similar to the finding that several other Class 0/I systems are currently accreting at rates which are not significant over the 0.5 Myr protostellar lifetime (Hartmann et al. 2025).

Models of protostars which assume the evolution of luminosity to be determined by the evolution of envelope-disk mass infall alone, and decreasing on a ~ 0.5 Myr

time scale, take the rate of disk-star mass accretion to be proportional to the rate of envelope-disk infall (e.g. Offner & McKee 2011, Fischer et al. 2017). In such models, the luminosities in the Class 0 phase are dominated by the slowly-evolving steady disk-star accretion, and the dispersion of the observed luminosities at a given mass would be the result of different infall rates for objects with different final masses. It is otherwise if there is episodic, rapid modulation of disk-star accretion apart from the envelope-disk infall trend, as is canonically invoked for outbursts in YSOs (e.g. Kenyon et al. 1990; Muzerolle et al. 2005; Aspin et al. 2009; Caratti o Garatti et al. 2011; Fischer et al. 2012; Safron et al. 2015; Kóspál et al. 2017; Hillenbrand et al. 2018; Fischer et al. 2019; Contreras Peña et al. 2024; Kulkarni et al. 2024). Then the variability due to episodic accretion contributes to, and may even dominate, the luminosity dispersion and mass assembly (Dunham et al. 2010; Dunham & Vorobyov 2012; Zakri et al. 2022; Fischer et al. 2023). Current observations of protostars with measured masses are indeed suggestive of a bimodal distribution of luminosity at a given mass (Hartmann et al. 2025). I16253 fits the episodic-accretion picture: its small luminosity compared to other, otherwise similar protostars is due to it being in a phase of very small accretion rate between large accretion-rate episodes.

7. CONCLUSIONS

1. OH pure-rotational emission observed in I16253 is a fluorescent cascade, with the molecules produced in circum-protostellar material by UV dissociation of H₂O. Thereby we have indirectly detected the protostar’s accretion-powered UV.
2. Using the reddening of the observed OH and CO₂ emission to correct for extinction toward this gas, and the CO₂ emission to measure indirectly the (undetected) parent H₂O population, we obtain the accretion rate of I16253: $\dot{M}_a = (3.3 \pm 2.2) \times 10^{-10} M_\odot \text{ year}^{-1}$. The primary uncertainty in \dot{M}_a is in estimation of the number of H₂O molecules absorbing the UV.
3. I16253’s accretion rate \dot{M}_a is consistent with its small outflow rate \dot{M}_w , and with the observational trend centered on the canonical YSO outflow/accretion mass-flow ratio of 0.1.
4. The accretion rate of I16253 is small on the scale of Class 0 protostars, even the other low-mass Class 0 protostars also plotted in Figure 8; it is insufficient by far to form a protostar during a protostellar lifetime. We therefore have the first clear detection of a Class 0 protostar in a quiescent phase,

in which its luminosity is dominated by the intrinsic luminosity of the central star. This discovery contributes to the growing body of evidence that Class 0 protostars undergo episodic accretion with large variation of accretion rates.

8. ACKNOWLEDGMENTS

We are grateful to Klaus Pontoppidan for providing the KP5 extinction model in advance of publication. We are also grateful to those who maintain the databases ancillary to this work: HITRAN, the NASA Astrophysical Data System, the Leiden Photodissociation and Photoionization database, and the Leiden Ice Database for Astrochemistry. This work is part of JWST general observing program 1802 (Investigating Prostellar Accretion); it is supported in part by NASA *via* the Space Telescope Science Institute. N.J.E. thanks the Astronomy Department of the University of Texas for research support. A.C.G. acknowledges support from PRIN-MUR 2022 20228JPA3A “The path to star and planet formation in the JWST era (PATH)”

funded by NextGeneration EU and by INAF-GoG 2022 “NIR-dark Accretion Outbursts in Massive Young stellar objects (NAOMY)” and Large Grant INAF 2022 “YSOs Outflows, Disks and Accretion: towards a global framework for the evolution of planet forming systems (YODA)”. C.P. acknowledges funding from the NSF Graduate Research Fellowship Program under grant No. DGE-1840990. A.S. gratefully acknowledges support by the Fondecyt Regular (project code 1220610), and ANID BASAL project FB210003. Part of this research by MN was carried out at the Jet Propulsion Laboratory, California Institute of Technology, under a contract with the National Aeronautics and Space Administration (80NM0018D0004).

Facility: JWST (MIRI)

DATA AVAILABILITY

All the data we present in this article were obtained from the Mikulski Archive for Space Telescopes (MAST) at the Space Telescope Science Institute. The specific observations can be accessed via [DOI: 10.17909/3kkyt040](https://doi.org/10.17909/3kkyt040).

APPENDIX

A. MID-INFRARED SPECTROSCOPY OF HYDROXYL AND CARBON DIOXIDE

OH. OH’s unpaired electron, specifically its electron-spin – electron-orbit interaction (i.e. fine structure), splits the OH ground electronic configuration (X) into two components, $X^2\Pi_{3/2}$ (X1.5) and $X^2\Pi_{1/2}$ (X0.5), as shown in Figure 3. The coupling of OH’s angular momentum components conforms well to Hund’s Case B (e.g. [Townes & Schawlow 1975](#), chapter 7). Each rotational state within each vibrational manifold of X1.5 and X0.5 is further split by the interaction of the unpaired electron’s spin with molecular rotation (i.e. Λ -type doubling) into two states with opposite total parity but the same total angular momentum quantum number J . Conventionally either the “rotationless” parity, labelled e or f , or the wavefunction symmetry/antisymmetry about the OH rotational plane, labelled A' and A'' , is specified for the Λ -doublet states, as either is conserved in rotational transitions, whereas total parity changes in the transitions. Antisymmetric, A'' states lie higher in energy than the symmetric, A' states. For the range of concern here, f states lie higher in energy than e for X1.5, and *vice versa* for X0.5. The molecular total orbital angular momentum $N\hbar$ — including rotation, but not electron spin — is approximately conserved, with its index $N = J \pm 1/2$ serving as a good quantum number. The selection rules for OH’s electric dipole transitions are thus $\Delta N = \pm 1, 0$ but no $0 \leftrightarrow 0$, and no $A'' \rightleftharpoons A'$. Each transition ΔN corresponds to a quartet of OH lines, as in Figures 2 and 3.

CO₂. See [Townes & Schawlow \(1975\)](#), chapter 2, for nomenclature. Each of the ro-vibration lines of CO₂ is split into two components by ℓ -type doubling, which are spectrally unresolved in our observations. The symmetry of CO₂, and the zero spin of the oxygen nuclei, forbid odd values of the total angular momentum quantum number J in the ground vibrational state, $\nu_1\nu_2\nu_3 = 00^00$.

B. THE FRACTION OF UV PHOTONS ABSORBED BY WATER

B.1. *Scenario ii: carbon dioxide and water in the hot core of I16253*

Here we take the observed gas-phase CO₂ to lie along the innermost parts of I16253’s outflow-cavity wall, as in a protostellar hot core. In Section 5.3, we take the rotation-vibration states of the CO₂ lines to be populated thermally, and calculate the extinction-corrected number and LTE temperature of the molecules (Table 1), whence the number of water molecules in the population is simply

$$n_{\text{H}_2\text{O}}(ii) = \frac{\mathcal{N}(\text{H}_2\text{O})}{\mathcal{N}(\text{CO}_2)} n_{\text{CO}_2} = (3.0 \pm 1.0) \times 10^{44} \text{ molecules} . \quad (\text{B1})$$

LTE is not an unreasonable initial assumption in light of the large mass of I16253's envelope ($1 M_{\odot}$), the consequent large density of the protostellar core, and current incompleteness in molecular-physics data which would be needed in a more detailed model. Assuming radiative equilibrium for dust grains, and gas heated by collisions with dust, the $T = 110$ K molecules lie approximately $r_{in} = 2.5$ AU from the central star. Models of Class 0 envelopes by Kristensen et al. (2012) typically have power-law density profile with index $p = 1.5$, and outer-to-inner radius ratio $Y = r_{out}/r_{in} = 1000$. Application of these parameters to I16253 gives hydrogen number density $\sim 5 \times 10^{10} \text{ cm}^{-3}$ at $r = r_{in}$ — indeed large on the scale of hot cores — and containin $n_{\text{H}_2} \sim 7 \times 10^{52}$ hydrogen molecules in the innermost warm zone in which most ices are completely sublimated ($T \geq 90$ K).

LTE also assumes that infrared pumping does not substantially affect the populations of the CO_2 rotation-vibration states, as it does in many hot cores (e.g. van Gelder et al. 2024b). We can check this by considering the continuum brightness temperature T_b of I16253 at the CO_2 lines' frequencies ($\lambda \sim 15 \mu\text{m}, \nu \sim 2 \times 10^{13} \text{ Hz}$). Correcting the observed flux density (1.8 mJy) for extinction toward and distance to I16253's central few AU to give the continuum surface brightness I_{ν} , we get

$$T_b = \frac{h\nu}{k} \frac{1}{\ln\left(1 + \frac{2h\nu^3}{c^2 I_{\nu}}\right)} = 45 \text{ K} , \quad (\text{B2})$$

small enough compared to the LTE excitation temperature of $T = 110$ K to conclude that infrared pumping can be neglected in first approximation.

Observations (e.g. van Dishoeck et al. 2021, van Gelder et al. 2024a) and models (e.g. Notsu et al. 2021) typically give $\text{H}_2\text{O}/\text{H}_2 \sim 10^{-7} - 10^{-5}$ in the inner parts of hot cores. The models also show that $\text{H}_2\text{O}/\text{H}_2$ and CO_2/H_2 are suppressed in hot cores relative to elsewhere in the protostars' envelopes, which is understood as due to X-ray dissociation of these molecules. A rough estimate based on Equation B1, and the envelope/innermost-warm-zone parameters of I16253, compare well to these results: we obtain $\text{H}_2\text{O}/\text{H}_2 \sim 4 \times 10^{-7}$. The hot-core models by Notsu et al. are optimized for protostars significantly more massive than I16253, and there have been no X-ray observations of I16253, so the models may not apply accurately here. However, it is not unusual in the model results for the interior $\text{H}_2\text{O}/\text{CO}_2$ relative abundance to resemble that of the colder outer parts of the envelope (Notsu et al. 2021, figures 3 and C.1). It is therefore not unreasonable to use the CO_2 ice feature's $\text{H}_2\text{O}/\text{CO}_2$ relative abundance in Equation B1.

Accurate calculations of collisional excitation rate coefficients for the rotation-vibration states of CO_2 are forthcoming (Selim et al. 2023), which will allow precise modeling of the molecular abundances in the core of I16253 in future articles.

B.2. Scenario iii: carbon dioxide and water photodesorbed from icy solids near the center of I16253

Next we consider the emitting medium to consist of gas recently released from icy solids, and calculate $n_{\text{H}_2\text{O}}$ from the observed CO_2 gas and ice, corrected for the rates of photoproduction and photolysis of H_2O and CO_2 . Again we neglect extinction between the central star and the icy solids associated with CO_2 and OH emission.

According to the CO_2 ice feature shape (Figure 4), H_2O and CO_2 are present in I16253's icy solids in the ratio $\mathcal{N}(\text{H}_2\text{O})/\mathcal{N}(\text{CO}_2) = 1.9$. However, the two gas species are not released from the solids at similar rates, nor do they have the same photolysis lifetime, so we need to make two corrections in order to calculate the steady-state number of water molecules $n_{\text{H}_2\text{O}}$ from n_{CO_2} . At the temperature obtained in the fit shown in Figure 4, H_2O and CO_2 ice would sublimate or thermally desorb at negligibly small rates (Minissale et al. 2022). But both species are readily photodesorbed by far-UV light. The desorption probability per UV photon, $p(\lambda)$, is calculated for H_2O by Andersson & van Dishoeck (2008), and measured for CO_2 by Fillion et al. (2014), whence a species' photodesorption rate q_{mol} is determined from our accretion-model flux λF_{λ} at system distance d_0 , for the solids' stellocentric distance r :

$$q_{mol}(p, F_{\lambda}) = \frac{1}{hc} \frac{d_0^2}{r^2} \int \lambda F_{\lambda}(\lambda) p(\lambda) d\lambda \quad (\text{B3})$$

The integral is over all wavelengths. Ratios of q_{mol} turn out to be independent of accretion rate for our model grid.

Photodissociation and photoionization cross sections are given for H_2O , OH and CO_2 by Fillion et al. (2003), van Dishoeck & Dalgarno (1984), and Huestis & Berkowitz (2010) respectively. Heays et al. (2017) parse the photodisso-

ciation cross section of H_2O into components with specific products, including $\text{OH}(X^2\Pi) + \text{H}$ ³⁸. In turn this latter cross-section component separates cleanly into the FAB and SAB, yielding the cross section σ_{SAB} which gives rise to OH rotational fluorescence.

In analogy with Equation B3, a species' total photolysis rate per molecule, Q_{mol} , is

$$Q_{mol}(\sigma_t, F_\lambda) = \frac{1}{hc} \frac{d_0^2}{r^2} \int \lambda F_\lambda(\lambda) \sigma_t(\lambda) d\lambda , \quad (\text{B4})$$

where $\sigma_t(\lambda)$ the sum of the molecule's photodissociation and photoionization cross sections. Using the $\dot{M}_a = 10^{-9} M_\odot \text{ year}^{-1}$ accretion model for example, we obtain photolysis lifetimes $1/Q_{\text{H}_2\text{O}} = 5.4 \times 10^3 \text{ sec}$, $1/Q_{\text{OH}} = 1.7 \times 10^4 \text{ sec}$, and $1/Q_{\text{CO}_2} = 2.3 \times 10^5 \text{ sec}$ for H_2O , OH , and CO_2 respectively. Thus, under conditions likely to prevail in I16253, H_2O is most rapidly destroyed of the three species; OH decays in its fluorescent cascade to small values of N long before being destroyed; and CO_2 , outlasting both, subsists long enough to serve as a proxy for the parent H_2O . As also is true for q_{mol} , ratios of Q_{mol} turn out to be independent of accretion rate for our model grid.

Thus the steady-state number of molecules in the parent H_2O population, within the photolysis lifetime after release from the ice, is

$$n_{\text{H}_2\text{O}}(iii) = \frac{\mathcal{N}(\text{H}_2\text{O})}{\mathcal{N}(\text{CO}_2)} \frac{q_{\text{H}_2\text{O}}}{q_{\text{CO}_2}} \frac{Q_{\text{CO}_2}}{Q_{\text{H}_2\text{O}}} n_{\text{CO}_2} = (1.9)(71.2)(0.0237)n_{\text{CO}_2} = (5.1 \pm 1.9) \times 10^{44} , \quad (\text{B5})$$

within uncertainties of $n_{\text{H}_2\text{O}}(ii)$. Note that the dependence on stellocentric distance r has canceled out, as usual for processes initiated by single photons. The irradiated and desorbed dust grains could lie anywhere SAB UV can reach within the unresolved source ($r < 40\text{AU}$). In this case the temperature T determined from the fit to the spectral-line fluxes would be characteristic of the kinetic energy ΔE of the CO_2 molecules upon UV-induced release from the dust grains, for which $\Delta E/k = 110 \text{ K}$ would not be unreasonable.

³⁸ See <https://home.strw.leidenuniv.nl/~ewine/photo/>.

Table 2. $\lambda = 10 - 26 \mu\text{m}$ spectral line fluxes within 1 arcsec of I16253

Wavelength μm	Species and transition (see endnotes for description)				Observed flux, $10^{-17} \text{ erg sec}^{-1} \text{ cm}^{-2}$			Extinction factor	
	1	2	3	4	5	6	7	8	
10.060	OH	X1.5	33	A''	<	0.2		49.6	\pm 21.9
10.062	OH	X0.5	33	A''	<	0.2		49.6	\pm 21.9
10.069	OH	X1.5	33	A'	+	1.9	\pm 0.1	49.5	\pm 21.8
10.071	OH	X0.5	33	A'					
10.221	OH	X1.5	32	A''	<	0.2		46.9	\pm 20.4
10.224	OH	X0.5	32	A''	<	0.1		46.8	\pm 20.3
10.231	OH	X1.5	32	A'	+	2.05	\pm 0.04	46.8	\pm 20.3
10.233	OH	X0.5	32	A'					
10.399	OH	X1.5	31	A''	<	0.2		43.2	\pm 18.4
10.402	OH	X0.5	31	A''	<	0.2		43.1	\pm 18.3
10.410	OH	X1.5	31	A'	+	3.20	\pm 0.05	42.8	\pm 18.2
10.412	OH	X0.5	31	A'					
10.595	OH	X1.5	30	A''	<	0.2		37.6	\pm 15.4
10.598	OH	X0.5	30	A''	<	0.2		37.4	\pm 15.3
10.607	OH	X1.5	30	A'	+	2.53	\pm 0.04	37.2	\pm 15.2
10.609	OH	X0.5	30	A'					
10.681	[Ni II]	$^4F_{7/2} - ^4F_{9/2}$				6.07	\pm 0.03	35.5	\pm 14.3
10.810	OH	X1.5	29	A''	<	0.1		32.7	\pm 12.9
10.815	OH	X0.5	29	A''	<	0.1		32.6	\pm 12.8
10.823	OH	X1.5	29	A'		2.7	\pm 0.1	32.5	\pm 12.8
10.826	OH	X0.5	29	A'		2.1	\pm 0.1	32.4	\pm 12.8
11.047	OH	X1.5	28	A''	<	0.2		29.7	\pm 11.4
11.052	OH	X0.5	28	A''	<	0.1		29.7	\pm 11.4
11.061	OH	X1.5	28	A'	+	1.65	\pm 0.04	29.7	\pm 11.4
11.065	OH	X0.5	28	A'					
11.307	[Ni I]	$^3F_2 - ^3F_3$				< 0.1		27.2	\pm 10.2
11.308	OH	X1.5	27	A''	<	0.1		27.2	\pm 10.2
11.313	OH	X0.5	27	A''	<	0.1		27.1	\pm 10.1
11.323	OH	X1.5	27	A'	+	3.1	\pm 0.1	27.0	\pm 10.1
11.327	OH	X0.5	27	A'					
11.333	[Cl I]	$^2P_{1/2} - ^2P_{3/2}$				3.2	\pm 0.1	26.7	\pm 9.9
11.594	OH	X1.5	26	A''	<	0.2		25.1	\pm 9.1
11.600	OH	X0.5	26	A''	<	0.2		24.9	\pm 9.1
11.610	OH	X1.5	26	A'		2.5	\pm 0.1	24.8	\pm 9.0
11.615	OH	X0.5	26	A'		2.7	\pm 0.1	24.8	\pm 9.0

Table 2 *continued*

Table 2 (continued)

Wavelength μm	Species and transition (see endnotes for description)				Observed flux, 10 ⁻¹⁷ erg sec ⁻¹ cm ⁻²			Extinction factor	
1	2	3	4	5	6	7		8	
11.909	OH	X1.5	25	<i>A''</i>	< 0.1		22.1	±	7.7
11.916	OH	X0.5	25	<i>A''</i>	< 0.1		22.1	±	7.7
11.926	OH	X1.5	25	<i>A'</i>	1.54	± 0.02	22.1	±	7.7
11.931	OH	X0.5	25	<i>A'</i>	2.05	± 0.02	22.1	±	7.7
12.256	OH	X1.5	24	<i>A''</i>	0.53	± 0.02	18.8	±	6.2
12.264	OH	X0.5	24	<i>A''</i>	0.85	± 0.02	18.7	±	6.2
12.274	OH	X1.5	24	<i>A'</i>	2.7	± 0.5	18.6	±	6.1
12.279	H ₂	<i>v</i> = 0	S 2		13.19	± 0.02	18.5	±	6.1
12.280	OH	X0.5	24	<i>A'</i>	4.3	± 0.9	18.5	±	6.1
12.372	H I	Hu α			< 0.1		17.8	±	5.8
12.638	OH	X1.5	23	<i>A''</i>	< 0.1		15.6	±	4.8
12.647	OH	X0.5	23	<i>A''</i>	< 0.1		15.5	±	4.8
12.657	OH	X1.5	23	<i>A'</i>	2.93	± 0.02	15.4	±	4.8
12.665	OH	X0.5	23	<i>A'</i>	2.84	± 0.02	15.4	±	4.8
12.728	[Ni II]	$^4F_{5/2} - ^4F_{7/2}$			2.24	± 0.02	14.9	±	4.5
12.812	[Ne II]	$^2P_{1/2} - ^2P_{3/2}$			29.21	± 0.02	14.2	±	4.3
13.060	OH	X1.5	22	<i>A''</i>	< 0.1		12.7	±	3.7
13.071	OH	X0.5	22	<i>A''</i>	0.40	± 0.02	12.6	±	3.6
13.081	OH	X1.5	22	<i>A'</i>	3.05	± 0.02	12.5	±	3.6
13.089	OH	X0.5	22	<i>A'</i>	2.59	± 0.02	12.4	±	3.5
13.527	OH	X1.5	21	<i>A''</i>	0.68	± 0.04	10.3	±	2.7
13.540	OH	X0.5	21	<i>A''</i>	1.16	± 0.04	10.2	±	2.7
13.549	OH	X1.5	21	<i>A'</i>	5.15	± 0.04	10.2	±	2.7
13.560	OH	X0.5	21	<i>A'</i>	5.14	± 0.04	10.2	±	2.7
14.045	OH	X1.5	20	<i>A''</i>	< 0.5		8.7	±	2.1
14.061	OH	X0.5	20	<i>A''</i>	0.92	± 0.05	8.7	±	2.1
14.069	OH	X1.5	20	<i>A'</i>	4.0	± 0.1	8.7	±	2.1
14.082	OH	X0.5	20	<i>A'</i>	4.22	± 0.03	8.6	±	2.1
14.621	CO ₂	01 ¹ 0 - 00 ⁰ 0	R 20		0.84	± 0.03	8.4	±	2.0
14.622	OH	X1.5	19	<i>A''</i>	0.92	± 0.03	8.4	±	2.0
14.641	OH	X0.5	19	<i>A''</i>	0.7	± 0.1	8.4	±	2.0
14.648	OH	X1.5	19	<i>A'</i>	4.26	± 0.03	8.4	±	2.0
14.655	CO ₂	01 ¹ 0 - 00 ⁰ 0	R 18		1.16	± 0.03	8.3	±	2.0
14.664	OH	X0.5	19	<i>A'</i>	4.31	± 0.03	8.3	±	2.0
14.689	CO ₂	01 ¹ 0 - 00 ⁰ 0	R 16		0.82	± 0.03	8.4	±	2.0
14.724	CO ₂	01 ¹ 0 - 00 ⁰ 0	R 14		1.34	± 0.03	8.6	±	2.1
14.758	CO ₂	01 ¹ 0 - 00 ⁰ 0	R 12		1.56	± 0.03	9.1	±	2.3

Table 2 continued

Table 2 (continued)

Wavelength μm	Species and transition (see endnotes for description)			Observed flux, 10 ⁻¹⁷ erg sec ⁻¹ cm ⁻²		Extinction factor		
1	2	3	4	5	6	7	8	
14.792	CO ₂	01 ¹ 0 – 00 ⁰ 0	R 10	1.75	± 0.03	9.6	± 2.5	
14.827	CO ₂	01 ¹ 0 – 00 ⁰ 0	R 8	1.87	± 0.03	10.4	± 2.7	
14.862	CO ₂	01 ¹ 0 – 00 ⁰ 0	R 6	1.97	± 0.03	10.8	± 2.9	
14.897	CO ₂	01 ¹ 0 – 00 ⁰ 0	R 4	1.54	± 0.03	11.4	± 3.2	
14.931	CO ₂	01 ¹ 0 – 00 ⁰ 0	R 2	0.55	± 0.03	11.8	± 3.3	
14.966	CO ₂	01 ¹ 0 – 00 ⁰ 0	R 0	1.06	± 0.03	12.3	± 3.5	
14.982	CO ₂	01 ¹ 0 – 00 ⁰ 0	Q branch	9.37	± 0.05	12.5	± 3.6	
15.019	CO ₂	01 ¹ 0 – 00 ⁰ 0	P 2	0.34	± 0.03	13.1	± 3.8	
15.054	CO ₂	01 ¹ 0 – 00 ⁰ 0	P 4	0.51	± 0.03	13.6	± 4.0	
15.090	CO ₂	01 ¹ 0 – 00 ⁰ 0	P 6	0.92	± 0.03	14.1	± 4.2	
15.125	CO ₂	01 ¹ 0 – 00 ⁰ 0	P 8	0.93	± 0.03	14.3	± 4.3	
15.160	CO ₂	01 ¹ 0 – 00 ⁰ 0	P 10	0.40	± 0.03	14.3	± 4.3	
15.196	CO ₂	01 ¹ 0 – 00 ⁰ 0	P 12	0.48	± 0.03	14.1	± 4.2	
15.232	CO ₂	01 ¹ 0 – 00 ⁰ 0	P 14	0.11	± 0.03	13.8	± 4.1	
15.267	OH	X1.5	18	<i>A''</i>	0.34	± 0.03	13.5	± 4.0
15.291	OH	X0.5	18	<i>A''</i> +	2.05	± 0.03	13.0	± 3.8
15.295	OH	X1.5	18	<i>A'</i>				
15.314	OH	X0.5	18	<i>A'</i>	1.82	± 0.03	12.6	± 3.6
15.991	OH	X1.5	17	<i>A''</i>	0.85	± 0.03	8.4	± 2.0
16.020	OH	X0.5	17	<i>A''</i> +	4.36	± 0.03	8.4	± 2.0
16.021	OH	X1.5	17	<i>A'</i>			8.4	± 2.0
16.045	OH	X0.5	17	<i>A'</i>	3.12	± 0.03	8.4	± 2.0
16.808	OH	X1.5	16	<i>A''</i>	1.6	± 0.03	8.7	± 2.1
16.840	OH	X1.5	16	<i>A'</i> +	4.8	± 0.03	8.8	± 2.2
16.843	OH	X0.5	16	<i>A''</i>				
16.870	OH	X0.5	16	<i>A'</i>	3.20	± 0.03	8.8	± 2.2
17.035	H ₂	<i>v</i> = 0	S 1		7.52	± 0.03	8.9	± 2.2
17.734	OH	X1.5	15	<i>A''</i>	1.8	± 0.03	9.2	± 2.3
17.769	OH	X1.5	15	<i>A'</i>	4.1	± 0.03	9.3	± 2.3
17.779	OH	X0.5	15	<i>A''</i>	0.82	± 0.03	9.3	± 2.3
17.808	OH	X0.5	15	<i>A'</i>	4.07	± 0.03	9.3	± 2.3
17.934	[Fe II]	⁴ F _{7/2} – ⁴ F _{9/2}			173.90	± 0.02	9.2	± 2.3
18.792	OH	X1.5	14	<i>A''</i>	2.5	± 0.1	9.1	± 2.3
18.830	OH	X1.5	14	<i>A'</i>	6.7	± 0.1	9.1	± 2.3
18.849	OH	X0.5	14	<i>A''</i>	3.2	± 0.1	9.1	± 2.3
18.880	OH	X0.5	14	<i>A'</i>	5.7	± 0.1	9.1	± 2.3
20.009	OH	X1.5	13	<i>A''</i>	2.4	± 0.3	8.3	± 2.0

Table 2 continued

Table 2 (continued)

Wavelength μm		Species and transition (see endnotes for description)				Observed flux, 10 ⁻¹⁷ erg sec ⁻¹ cm ⁻²		Extinction factor	
1	2	3	4	5	6	7		8	
20.050	OH	X1.5	13	<i>A'</i>	5.4	± 0.3	8.3	± 2.0	
20.082	OH	X0.5	13	<i>A''</i>	3.3	± 0.3	8.2	± 2.0	
20.115	OH	X0.5	13	<i>A'</i>	7.4	± 0.3	8.2	± 1.9	
21.420	OH	X1.5	12	<i>A''</i>	5.2	± 0.5	7.1	± 1.6	
21.465	OH	X1.5	12	<i>A'</i>	11.7	± 0.5	7.1	± 1.6	
21.517	OH	X0.5	12	<i>A''</i>	3.9	± 0.5	7.0	± 1.6	
21.553	OH	X0.5	12	<i>A'</i>	8.9	± 0.5	7.0	± 1.5	
23.074	OH	X1.5	11	<i>A''</i>	7.6	± 0.8	6.1	± 1.2	
23.123	OH	X1.5	11	<i>A'</i>	22.9	± 0.8	6.1	± 1.2	
23.205	OH	X0.5	11	<i>A''</i>	9.9	± 0.9	6.0	± 1.2	
23.243	OH	X0.5	11	<i>A'</i>	19.4	± 0.8	6.0	± 1.2	
24.512	[Fe II]	$^4F_{5/2} - ^4F_{7/2}$			71.6	± 0.3	5.4	± 1.0	
25.035	OH	X1.5	10	<i>A''</i>	12.3	± 0.3	5.2	± 1.0	
25.090	OH	X1.5	10	<i>A'</i>	32.1	± 0.3	5.2	± 1.0	
25.216	OH	X0.5	10	<i>A''</i>	15.5	± 0.3	5.2	± 1.0	
25.251	[S I]	$^3P_1 - ^3P_2$			77.9	± 0.3	5.2	± 1.0	
25.258	OH	X0.5	10	<i>A'</i>	39.9	± 8.0	5.2	± 1.0	
25.989	[Fe II]	$^6F_{7/2} - ^6F_{9/2}$			268.8	± 0.5	4.9	± 0.9	

³For OH, electronic configuration; X1.5 = $X^2\Pi_{3/2}$ and X0.5 = $X^2\Pi_{1/2}$. For CO₂, vibrational quantum numbers $\nu_1\nu_2^l\nu_2$ of initial and final state. For H₂, vibrational quantum number. For ions and atoms, initial and final electron configuration in $^{2S+1}L_J$ form.

⁴For OH, lower-state orbital angular momentum quantum number *N*. For CO₂, rotational transition identification, with P-Q-R signifying $\Delta J = +1, 0, -1$, and a numeral for lower-state total angular momentum quantum number *J*.

⁵For OH, symmetry (*A'*) or antisymmetry (*A''*) of wavefunction about molecular orbital plane.

⁶“+” indicates a transition spectrally unresolved from the following one. Its fluxes (7) and extinction factors (8) apply to the unresolved combination.

⁷Line flux $\pm 1\sigma$ uncertainty, or 3σ upper limit.

⁸Extinction correction factors and their uncertainties, derived as per Section 5.3. The factor is multiplied with the observed flux, and the uncertainty propagated with that of the observed flux, to produce extinction-corrected values in the analysis.

NOTE—Lines not listed are not detected. Upper limits may be calculated by interpolation among the entries of columns 1 and 7.

REFERENCES

Alcalá, J. M., Natta, A., Manara, C. F., et al. 2014, *A&A*, 561, A2

Alcalá, J. M., Manara, C. F., Natta, A., et al. 2017, *A&A*, 600, A20

Alexander, M. H., Rackham, E. J., & Manolopoulos, D. E. 2004, *JChPh*, 121, 5221

Andersson, S., & van Dishoeck, E. F. 2008, *A&A*, 491, 907

Andresen, P., Ondrey, G. S., Titze, B., & Rothe, E. W. 1984, *JChPh*, 80, 2548

Aso, Y., Kwon, W., Ohashi, N., et al. 2023, *ApJ*, 954, 101

Aspin, C., Reipurth, B., Beck, T. L., et al. 2009, *ApJL*, 692, L67

Barsony, M., Wolf-Chase, G. A., Ciardi, D. R., & O'Linger, J. 2010, *ApJ*, 720, 64

Bastien, P. 1982, *A&AS*, 48, 153

Bohren, C. F., & Huffman, D. R. 1998, *Absorption and Scattering of Light by Small Particles* (Wiley-VCH)

Bonev, B. P., & Mumma, M. J. 2006, *ApJ*, 653, 788

Brooke, J. S. A., Bernath, P. F., Western, C. M., et al. 2016, *JQSRT*, 168, 142

Brunken, N. G. C., Boogert, A. C. A., van Dishoeck, E. F., et al. 2025, arXiv e-prints, arXiv:2505.14769

Calvet, N., & Gullbring, E. 1998, *ApJ*, 509, 802

Caratti o Garatti, A., Garcia Lopez, R., Scholz, A., et al. 2011, *A&A*, 526, L1

Carr, J. S., & Najita, J. R. 2011, *ApJ*, 733, 102

—. 2014, *ApJ*, 788, 66

Chang, Y., Yu, Y., Wang, H., et al. 2019, *Nature Communications*, 10, 1250

Chapman, N. L., Mundy, L. G., Lai, S.-P., & Evans, Neal J., I. 2009, *ApJ*, 690, 496

Contreras Peña, C., Lucas, P. W., Guo, Z., & Smith, L. 2024, *MNRAS*, 528, 1823

Crovisier, J. 1989, *A&A*, 213, 459

Dixon, R. N. 1995, *JChPh*, 102, 301

Dunham, M. M., Evans, Neal J., I., Terebey, S., Dullemond, C. P., & Young, C. H. 2010, *ApJ*, 710, 470

Dunham, M. M., & Vorobyov, E. I. 2012, *ApJ*, 747, 52

Dunham, M. M., Stutz, A. M., Allen, L. E., et al. 2014, in *Protostars and Planets VI*, ed. H. Beuther, R. S. Klessen, C. P. Dullemond, & T. Henning, 195–218

Ehrenfreund, P., Boogert, A. C. A., Gerakines, P. A., Tielens, A. G. G. M., & van Dishoeck, E. F. 1997, *A&A*, 328, 649

Ehrenfreund, P., Kerkhof, O., Schutte, W. A., et al. 1999, *A&A*, 350, 240

Federman, S., Megeath, S. T., Tobin, J. J., et al. 2023, *ApJ*, 944, 49

Federman, S. A., Megeath, S. T., Rubinstein, A. E., et al. 2024, *ApJ*, 966, 41

Fillion, J. H., Dulieu, F., Baouche, S., et al. 2003, *Journal of Physics B Atomic Molecular Physics*, 36, 2767

Fillion, J.-H., Fayolle, E. C., Michaut, X., et al. 2014, *Faraday Discussions*, 168, 533

Fiorellino, E., Tychoniec, L., Cruz-Sáenz de Miera, F., et al. 2023, *ApJ*, 944, 135

Fischer, W. J., Hillenbrand, L. A., Herczeg, G. J., et al. 2023, in *Astronomical Society of the Pacific Conference Series*, Vol. 534, *Protostars and Planets VII*, ed. S. Inutsuka, Y. Aikawa, T. Muto, K. Tomida, & M. Tamura, 355

Fischer, W. J., Safron, E., & Megeath, S. T. 2019, *ApJ*, 872, 183

Fischer, W. J., Megeath, S. T., Tobin, J. J., et al. 2012, *ApJ*, 756, 99

Fischer, W. J., Megeath, S. T., Furlan, E., et al. 2017, *ApJ*, 840, 69

France, K., Schindhelm, R., Bergin, E. A., Roueff, E., & Abgrall, H. 2014, *ApJ*, 784, 127

Grant, S. L., van Dishoeck, E. F., Tabone, B., et al. 2023, *ApJL*, 947, L6

Gullbring, E., Hartmann, L., Briceño, C., & Calvet, N. 1998, *ApJ*, 492, 323

Harich, S. A., Hwang, D. W. H., Yang, X., et al. 2000, *JChPh*, 113, 10073

Hartigan, P., Edwards, S., & Ghandour, L. 1995, *ApJ*, 452, 736

Hartmann, L. 2009, *Accretion Processes in Star Formation*: Second Edition (Cambridge University Press)

Hartmann, L., Herczeg, G., & Calvet, N. 2016, *ARA&A*, 54, 135

Hartmann, L., Tobin, J. J., Sheehan, P., Kounkel, M., & Zhao, C. 2025, *MNRAS*, arXiv:2507.18728

Heays, A. N., Bosman, A. D., & van Dishoeck, E. F. 2017, *A&A*, 602, A105

Hillenbrand, L. A., Contreras Peña, C., Morrell, S., et al. 2018, *ApJ*, 869, 146

Hsieh, T.-H., Hirano, N., Belloche, A., et al. 2019, *ApJ*, 871, 100

Hsieh, T.-H., Lai, S.-P., & Belloche, A. 2017, *AJ*, 153, 173

Huestis, D. L., & Berkowitz, J. 2010, in *AAS/Division for Planetary Sciences Meeting Abstracts*, Vol. 42, *AAS/Division for Planetary Sciences Meeting Abstracts* #42, 48.13

Husser, T. O., Wende-von Berg, S., Dreizler, S., et al. 2013, *A&A*, 553, A6

Kalugina, Y., Lique, F., & Marinakis, S. 2014, *Physical Chemistry Chemical Physics (Incorporating Faraday Transactions)*, 16, 13500

Kenyon, S. J., Hartmann, L. W., Strom, K. M., & Strom, S. E. 1990, *AJ*, 99, 869

Komarova, O., & Fischer, W. J. 2020, *Research Notes of the American Astronomical Society*, 4, 6

Kóspál, Á., Ábrahám, P., Csengeri, T., et al. 2017, *ApJ*, 843, 45

Kristensen, L. E., van Dishoeck, E. F., Bergin, E. A., et al. 2012, *A&A*, 542, A8

Kulkarni, C. S., Behling, T., Burns-Watson, N., et al. 2024, *Research Notes of the American Astronomical Society*, 8, 64

Le Gouellec, V. J. M., Greene, T. P., Hillenbrand, L. A., & Yates, Z. 2024, *ApJ*, 966, 91

Liu, X., Lin, J. J., Harich, S., Schatz, G. C., & Yang, X. 2000, *Science*, 289, 1536

Menu, J., van Boekel, R., Henning, T., et al. 2014, *A&A*, 564, A93

Minissale, M., Aikawa, Y., Bergin, E., et al. 2022, *ACS Earth and Space Chemistry*, 6, 597

Mordaunt, D. H., Ashfold, M. N. R., & Dixon, R. N. 1994, *JChPh*, 100, 7360

Muzerolle, J., Calvet, N., & Hartmann, L. 2001, *ApJ*, 550, 944

Muzerolle, J., Hartmann, L., & Calvet, N. 1998, *AJ*, 116, 2965

Muzerolle, J., Megeath, S. T., Flaherty, K. M., et al. 2005, *ApJL*, 620, L107

Najita, J. R., Carr, J. S., Strom, S. E., et al. 2010, *ApJ*, 712, 274

Narang, M., Manoj, P., Tyagi, H., et al. 2024, *ApJL*, 962, L16

Neufeld, D. A., Manoj, P., Tyagi, H., et al. 2024, *ApJL*, 966, L22

Noll, S., Winkler, H., Goussov, O., & Proxauf, B. 2020, *Atmospheric Chemistry & Physics*, 20, 5269

Notsu, S., van Dishoeck, E. F., Walsh, C., Bosman, A. D., & Nomura, H. 2021, *A&A*, 650, A180

Offer, A. R., van Hemert, M. C., & van Dishoeck, E. F. 1994, *JChPh*, 100, 362

Offner, S. S. R., & McKee, C. F. 2011, *ApJ*, 736, 53

Ohashi, S., Momose, M., Kataoka, A., et al. 2023, *ApJ*, 954, 110

Pelletier, G., & Pudritz, R. E. 1992, *ApJ*, 394, 117

Pittman, C. V., Espaillat, C. C., Robinson, C. E., et al. 2022, *AJ*, 164, 201

—. 2025, arXiv e-prints, arXiv:2507.01162

Pokhrel, R., Megeath, S. T., Gutermuth, R. A., et al. 2023, *ApJS*, 266, 32

Pontoppidan, K. M., Evans, N., Bergner, J., & Yang, Y.-L. 2024, *Research Notes of the American Astronomical Society*, 8, 68

Pontoppidan, K. M., Salyk, C., Blake, G. A., et al. 2010, *ApJ*, 720, 887

Pontoppidan, K. M., Boogert, A. C. A., Fraser, H. J., et al. 2008, *ApJ*, 678, 1005

Riaz, B., & Bally, J. 2021, *MNRAS*, 501, 3781

Robinson, C. E., & Espaillat, C. C. 2019, *ApJ*, 874, 129

Rocha, W. R. M., McClure, M. K., Sturm, J. A., et al. 2025, *A&A*, 693, A288

Rubinstein, A. E., Evans, N. J., Tyagi, H., et al. 2024, *ApJ*, 974, 112

Safron, E. J., Fischer, W. J., Megeath, S. T., et al. 2015, *ApJL*, 800, L5

Selim, T., van der Avoird, A., & Groenenboom, G. C. 2023, *JChPh*, 159, 164310

Shirley, Y. L., Huard, T. L., Pontoppidan, K. M., et al. 2011, *ApJ*, 728, 143

Stapelfeldt, K., Burrows, C. J., Krist, J. E., & WFPC2 Science Team. 1997, in *IAU Symposium*, Vol. 182, *Herbig-Haro Flows and the Birth of Stars*, ed. B. Reipurth & C. Bertout, 355–364

Tabone, B., van Dishoeck, E. F., & Black, J. H. 2024, arXiv e-prints, arXiv:2406.14560

Tabone, B., van Hemert, M. C., van Dishoeck, E. F., & Black, J. H. 2021, *A&A*, 650, A192

Tappe, A., Forbrich, J., Martín, S., Yuan, Y., & Lada, C. J. 2012, *ApJ*, 751, 9

Tappe, A., Lada, C. J., Black, J. H., & Muench, A. A. 2008, *ApJL*, 680, L117

Testi, L., Natta, A., Gozzi, S., et al. 2025, arXiv e-prints, arXiv:2506.14601

Tobin, J. J., Hartmann, L., Chiang, H.-F., et al. 2011, *ApJ*, 740, 45

Tofflemire, B. M., Manara, C. F., Banzatti, A., et al. 2025, *ApJ*, 985, 224

Townes, C. H., & Schawlow, A. L. 1975, *Microwave Spectroscopy*. (Dover Publications)

van Dishoeck, E. F., & Dalgarno, A. 1984, *Icarus*, 59, 305

van Dishoeck, E. F., Kristensen, L. E., Mottram, J. C., et al. 2021, *A&A*, 648, A24

van Gelder, M. L., Francis, L., van Dishoeck, E. F., et al. 2024a, *A&A*, 692, A197

—. 2024b, *A&A*, 692, A197

Vlasblom, M., Temmink, M., Grant, S. L., et al. 2025, *A&A*, 693, A278

Watson, D. M., Calvet, N. P., Fischer, W. J., et al. 2016, *ApJ*, 828, 52

Young, J. W., Booth, R. S., Vogelhuber, K. M., Stearns, J. A., & Annesley, C. J. 2018, *Journal of Physical Chemistry A*, 122, 5602

Young, K. E., Enoch, M. L., Evans, N. J. I., et al. 2006, *ApJ*, 644, 326

Zakri, W., Megeath, S. T., Fischer, W. J., et al. 2022, *ApJL*, 924, L23

Zannese, M., Tabone, B., Habart, E., et al. 2024, *Nature Astronomy*, 8, 577

Zasowski, G., Kemper, F., Watson, D. M., et al. 2009, *ApJ*, 694, 459

Zhou, L., Xie, D., & Guo, H. 2015, *JChPh*, 142, 124317